

DINO-SLAM: DINO-informed RGB-D SLAM for Neural Implicit and Explicit Representations

Ziren Gong^{*1}, Xiaohan Li^{*2}, Fabio Tosi¹, Youmin Zhang³, Stefano Mattoccia¹, Jun Wu⁴, Matteo Poggi¹

University of Bologna¹, USTC², Rock Universe³, Fudan University⁴

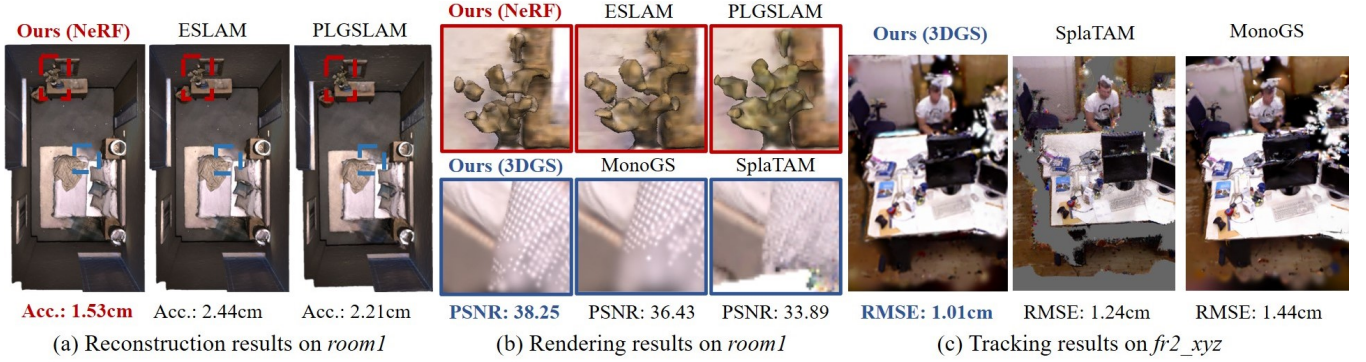


Figure 1: **Mapping, rendering, and tracking results on Replica *room1* (Straub et al. 2019) and TUM *fr2_xyz* (Sturm et al. 2012).** Our method produces the accurate 3D reconstruction shown in (a), along with more precise camera tracking in (c). Compared to existing methods such as PLGSLAM, ESLAM, SplaTAM, and MonoGS, DINO-SLAM better preserves completeness and detail (see red boxes and blue boxes), achieving superior reconstruction and rendering quality - see (b).

Abstract

This paper presents DINO-SLAM, a DINO-informed design strategy to enhance neural implicit (Neural Radiance Field – NeRF) and explicit representations (3D Gaussian Splatting – 3DGS) in SLAM systems through more comprehensive scene representations. Purposely, we rely on a Scene Structure Encoder (SSE) that enriches DINO features into Enhanced DINO ones (EDINO) to capture hierarchical scene elements and their structural relationships. Building upon it, we propose two foundational paradigms for NeRF and 3DGS SLAM systems integrating EDINO features. Our DINO-informed pipelines achieve superior performance on the Replica, ScanNet, and TUM compared to state-of-the-art methods.

1 Introduction

Dense simultaneous localization and mapping (SLAM) has emerged as a fundamental technology in robotics and autonomous systems, with extensive applications ranging from mobile robotics to autonomous vehicles. As a core component of spatial intelligence, dense SLAM enables real-time camera localization while constructing detailed environmental maps, thereby facilitating autonomous navigation and scene understanding. Initially, SLAM techniques were

primarily hand-crafted algorithms (Mur-Artal, Montiel, and Tardós 2015; Mur-Artal and Tardós 2017; Campos et al. 2021; Newcombe, Lovegrove, and Davison 2011; Salas-Moreno et al. 2013), facing limitations in the presence of challenging lighting conditions and poorly textured environments. The advent of deep learning has further advanced the field which significantly improves pose estimation accuracy through learned features and matching (Tateno et al. 2017; Li et al. 2020; Teed and Deng 2021), peaking with the recent breakthroughs in novel view synthesis, notably Neural Radiance Fields (NeRF) (Mildenhall et al. 2021) and 3D Gaussian Splatting (3DGS) (Kerbl et al. 2023), that have revolutionized this field with new, exciting possibilities. Nevertheless, current NeRF or 3DGS-based SLAM systems primarily focus on geometric reconstruction and photometric consistency, overlooking higher-level scene understanding necessary for complex scene representation and autonomous navigation. Indeed, these frameworks rely on supervisory signals coming from pixel-wise colors or depth, thus lacking such a higher-level understanding of both those local and global properties that conventional feed-forward vision models can encode in deep features (Caron et al. 2021).

In this paper we propose DINO-SLAM, a novel and general framework that seamlessly integrates the higher-level

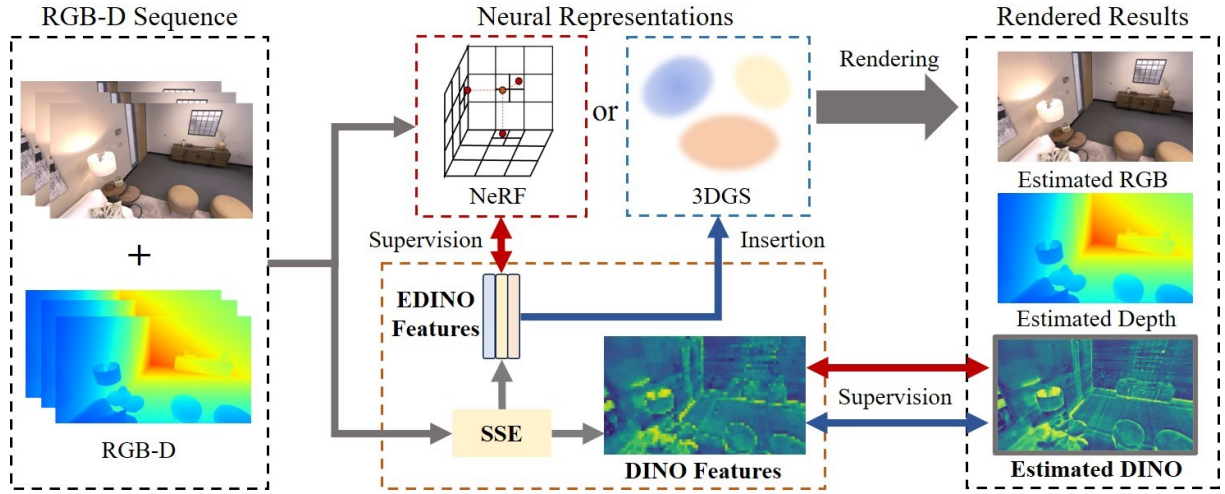


Figure 2: **Overview of DINO-SLAM for neural implicit or explicit representations.** Both neural representations share the same structure of **Scene Structure Encoder (SSE)** to capture enhanced-DINO (EDINO) and DINO features. In our neural implicit pipeline (NeRF), **EDINO features** provide supervision for the tri-plane optimization (red double arrow) while **DINO features** serve roles in guiding the optimization of the estimated DINO feature map (red double arrow). In our neural explicit pipeline (3DGS), we incorporate **EDINO features** into Gaussian parameters (arrow) and leverage **DINO features** to supervise the estimated feature map (blue double arrow).

scene understanding encoded in the features extracted by a self-supervised vision model (DINO (Caron et al. 2021)) into the SLAM system. DINO-SLAM offers three key advantages: i) hierarchical scene understanding; compared to existing SLAM methods, DINO-SLAM captures a comprehensive hierarchy of scene features (geometric details, part-level, and scene-level layouts), ii) capture of continuous features and structural relationships; rather than operating on discrete labels as in semantic SLAM, the continuous feature space enables DINO-SLAM to capture inter-component and part-whole relationships within scenes, and iii) a self-supervision model without requiring pre-defined categories and annotated labels needed for semantic SLAM. These properties make DINO-SLAM well-suited for neural scene representation in practical applications. The foundation of DINO-SLAM is a custom model, the *Scene Structure Encoder (SSE)*, that extracts a hierarchy of higher-level features encoding both contextual understanding and structural relationships starting from the original DINO features, lifting them into enhanced DINO (EDINO) features. Building upon this extractor, we establish two specialized paradigms suited for both NeRF-based and 3DGS-based SLAM methods. We demonstrate the wide applicability of our approach through integration with various scene-encoding SLAM methods (Wang, Wang, and Agapito 2023; Johari, Carta, and Fleuret 2023; Sandström et al. 2023; Keetha et al. 2024; Matsuki et al. 2024), over standard benchmarks in the field (Straub et al. 2019; Sturm et al. 2012; Dai et al. 2017), where our DINO-SLAM systems achieve state-of-the-art accuracy – as shown in Fig. 1. Our key contributions are:

- We introduce DINO-SLAM, a DINO-informed dense RGB-D SLAM system that achieves precise scene representation and robust tracking without requiring semantic annotations, pre-defined categories, or offline training.

- We develop a Scene Structure Encoder (SSE) that enriches scene representations with hierarchical scene features and structural relationships. Based on this, we implement two foundational paradigms suitable for both NeRF-based and 3DGS-based SLAM systems.
- We validate our wide applicability to neural implicit and explicit SLAM methods by integrating our SSE into various scene representations. Extensive experiments on popular datasets (Straub et al. 2019; Sturm et al. 2012; Dai et al. 2017) demonstrate the superior performance of our DINO-SLAM pipelines.

2 Related work

Here, we briefly review the research related to our work. More detailed literature can be found in (Tosi et al. 2024).

Neural Implicit SLAM. With the emergence of NeRF (Mildenhall et al. 2021), numerous methods (Sucar et al. 2021; Zhu et al. 2022; Johari, Carta, and Fleuret 2023; Wang, Wang, and Agapito 2023; Deng et al. 2024; Gong et al. 2025; Sandström et al. 2023) have incorporated such implicit volumetric representation into SLAM frameworks. As the first work using implicit neural representations for SLAM, iMAP (Sucar et al. 2021) adopts an MLP to map the 3D coordinates to color and volume density. NICE-SLAM (Zhu et al. 2022) further extends the single MLP of iMAP to a hierarchical structure, which improves the quality of dense reconstruction by optimizing a hierarchical representation. Current works further explore different scene encodings, such as hash-grid (Wang, Wang, and Agapito 2023; Zhang et al. 2023; Xin et al. 2024; Park et al. 2024), neural-point (Sandström et al. 2023; Liso et al. 2024; Hu et al. 2023), and tri-planes (Johari, Carta, and Fleuret 2023; Deng et al. 2024; Park et al. 2024), to enhance scene modeling

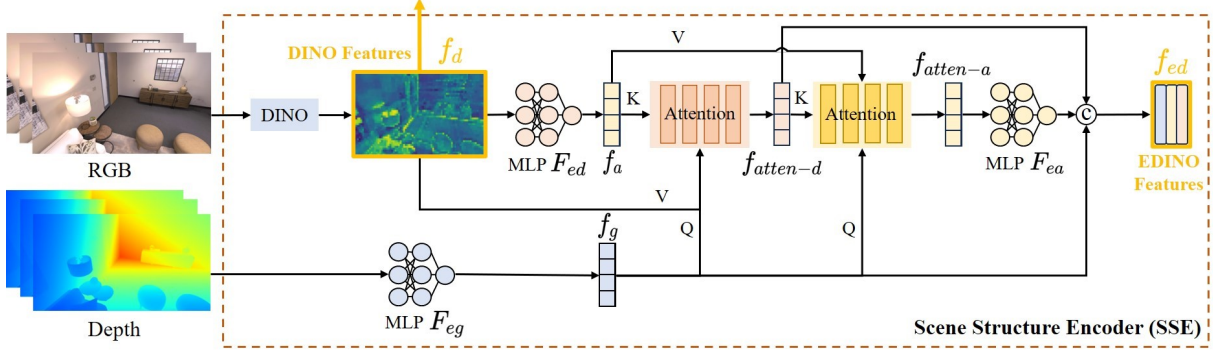


Figure 3: **The architecture of Scene Structure Encoder (SSE).** Our SSE has two outputs (in yellow): 1) **DINO features** f_d : Given the RGB frames, the self-supervised vision transformer (DINO) extracts self-attention features as one of the outputs. 2) **EDINO features** f_{ed} : We separately encode DINO features f_d and depth information into appearance f_a and geometric features f_g . These features, along with the extracted DINO features, undergo refinement based on their inter-relationships before being concatenated into comprehensive feature representations.

capabilities.

Neural Explicit SLAM. 3D Gaussian Splatting (3DGS) (Kerbl et al. 2023), as an explicit radiance field technique, has been recently widely used in SLAM methods. Compared to NeRF-based SLAM, these methods (Keetha et al. 2024; Yan et al. 2024; Yugay et al. 2023; Matsuki et al. 2024; Huang et al. 2024; Hu et al. 2024; Peng et al. 2024; Ha, Yeon, and Yu 2024; Zheng et al. 2025) offer two key advantages: explicit spatial extent mapping and local explicit mapping editability, enabling real-time adjustments and corrections of scene representations. As pioneers, MonoGS (Matsuki et al. 2024) incorporate 3DGS into RGB-D SLAM systems for efficient and high-quality rendering of environments. SplatTAM (Keetha et al. 2024) leverages a group of simplified Gaussians to represent the whole scene, GS-SLAM (Yugay et al. 2023) encodes both appearance and geometry by 3D Gaussians with opacity and spherical harmonics, while WildGS-SLAM (Zheng et al. 2025) learns to ignore moving objects and distractors through uncertainty.

So far, both implicit and explicit methods overlook the potential of the standalone DINO features and how their guidance can improve the accuracy of existing SLAM systems. In this paper, we comprehensively explore the advancement of DINO to SLAM systems with different scene representations, suggesting the potential to extend DINO features to future SLAM systems based on radiance fields.

3 Method Overview

We now introduce our DINO-SLAM framework, which supports both neural implicit and explicit representations, as illustrated in Figure 2.

3.1 Scene Structure Encoder

Given the strong priors encoded in DINO features (Caron et al. 2021), we design a Scene Structure Encoder (SSE) that further enriches these encodings by leveraging inter-relationships between DINO features, geometric understanding, and appearance information to generate more informative enhanced-DINO (EDINO) outputs. These cues

guide the scene modeling in our SLAM systems, removing bottlenecks caused by conventional color and depth pixel-wise supervisions. As shown in Figure 3, our encoder can be formalized as a model Φ_{SSE} that processes the color c and depth d to capture DINO f_d and EDINO features f_{ed} :

$$\Phi_{SSE}(c, d) \rightarrow (f_d, f_{ed}) \quad (1)$$

Specifically, DINO features obtained through the ViT-small architecture from (Caron et al. 2021) undergo further processing through a MLP F_{ed} to encode explicit information as appearance features f_a . Concurrently, depth sequences are processed by a separate MLP F_{eg} to extract geometric information f_g containing spatial relations and arrangements. These quantities, f_d , f_a , and f_g , are then refined through an attention module that exploits geometric-appearance relationships to enhance inter-component understanding:

$$f_{atten-d} = \text{softmax} \left(\frac{f_g f_a^T}{\sqrt{d_a}} \right) f_d \quad (2)$$

where $f_{atten-d}$ represents the refined DINO features guided by geometric and appearance information. d_a is the feature dimension of f_a . Given the strong correlation between DINO features and geometric components in capturing scene structures, we employ a second attention module to enhance appearance representation with part-whole relations:

$$f_{atten-a} = \text{softmax} \left(\frac{f_g f_{atten-d}^T}{\sqrt{d_{atten-d}}} \right) f_a \quad (3)$$

where $f_{atten-a}$ denotes the enhanced appearance features guided by relevant DINO and geometric information. $d_{atten-d}$ is the feature dimension of $f_{atten-d}$. These undergo further refinement through a MLP F_{ea} to produce $f'_{atten-a}$. Finally, we obtain the EDINO features f_{ed} as a concatenation of $[f'_{atten-a}, f_{atten-d}, f_g]$. Our experiments demonstrate that these higher-level encodings are crucial for optimal results, whereas embedding DINO features alone in SLAM pipelines yields suboptimal results.

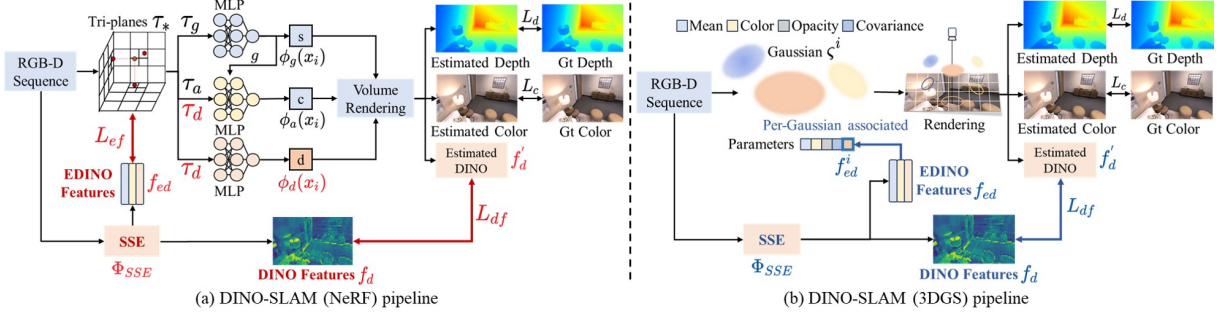


Figure 4: **Architectures of DINO-informed neural implicit (NeRF) and explicit (3DGS) SLAM pipelines.** In the NeRF-based pipeline (**left**), we leverage EDINO features f_{ed} to supervise the tri-plane τ_d (**red double arrow**) while DINO features f_d guide the optimization of the estimated DINO feature map f'_d (**red double arrow**). In the 3DGS-based pipeline (**right**), we incorporate the corresponding EDINO feature f_{ed}^i into the parameters of each Gaussian ζ^i (**blue arrow**). Meanwhile, the DINO features f_d are leveraged to guide the learning of DINO information within the representation (**blue double arrow**).

3.2 NeRF-based Pipeline

Building upon the SSE, we first design a NeRF-based version of DINO-SLAM, illustrated in Figure 4 (a).

Scene Representation. Our NeRF-based pipeline is optimized to render RGB, depth, and raw DINO features through ray sampling, leveraging the per-pixel ray casting property inherent to NeRF methods. As illustrated in Figure 4 (a), our framework encodes the sampled points x_i along the rays into tri-planes (Johari, Carta, and Fleuret 2023). Specifically, we design three distinct tri-planes (τ_g , τ_a , and τ_d) to separately learn geometric, appearance, and EDINO representations. Three shallow MLPs, each consisting of two fully-connected layers, then process these tri-plane encodings to produce the signed distance function (SDF) $\phi_g(x_i)$, raw colors $\phi_a(x_i)$, and raw DINO features $\phi_d(x_i)$. While the DINO features extracted from images supervise ϕ_d , the EDINO features from our SSE optimize the tri-plane encodings τ_d , as detailed in subsequent sections.

DINO-informed Rendering. We adopt the standard ray-casting process used in NeRF (Mildenhall et al. 2021). For all points sampled along a ray $\{p_n\}_{n=1}^N$, we query TSDF $\phi_g(p_n)$, raw color $\phi_a(p_n)$, and raw DINO features $\phi_d(p_n)$ from our MLPs. We then apply SDF-based rendering to compute volume densities:

$$\sigma(p_n) = \beta \cdot \text{Sigmoid}(-\beta \cdot \phi_g(p_n)) \quad (4)$$

where $\sigma(p_n)$ represents the volume density and β is a learnable parameter controlling the sharpness of the surface boundary. The termination probability w_n , color \hat{c}_n , depth \hat{d}_n , and estimated DINO features f'_d are rendered using these volume densities:

$$w_n = \exp\left(-\sum_{k=1}^{n-1} \sigma(p_k)\right) (1 - \exp(-\sigma(p_n)))$$

$$\text{with } f'_d = \sum_{n=1}^N w_n \phi_d(p_n) \quad (5)$$

$$\hat{c}_n = \sum_{n=1}^N w_n \phi_a(p_n), \quad \text{and} \quad \hat{d}_n = \sum_{n=1}^N w_n z_n \quad (6)$$

where z_n denotes the depth of sampled point p_n .

DINO-informed Supervision. We introduce two feature-level losses to enhance scene representation supervision. As shown in Figure 4 (a), we implement an encoding feature loss L_{ef} to supervise the tri-planes τ_d responsible for learning enriched spatial and appearance cues. This loss function computes the feature similarity between the tri-planes τ_d and the EDINO features f_{ed} :

$$L_{ef} = \|\tau_d - f_{ed}\|_1 \quad (7)$$

To optimize the DINO feature representation, we introduce a DINO-feature loss L_{df} :

$$L_{df} = \|f'_d - f_d\|_1 \quad (8)$$

Additionally, we employ standard color and depth losses:

$$L_c = \frac{1}{N} \sum_{n=1}^N (\hat{c}_n - c_n)^2, \quad L_d = \frac{1}{N} \sum_{n=1}^N (\hat{d}_n - d_n)^2 \quad (9)$$

where c_n and d_n represent the ground truth color and depth, respectively. We also incorporate additional loss terms from (Johari, Carta, and Fleuret 2023), including free space loss, signed distance loss, and truncation loss.

Mapping and Tracking. Following (Johari, Carta, and Fleuret 2023), our mapping process randomly samples R pixels from a temporal window comprising the current frame, the two most recent frames, and $W - 3$ frames selected from keyframes. Keyframes are systematically selected every k frames from the input RGB-D sequences. The training process jointly optimizes three components: the tri-planes (τ_g , τ_a , and τ_d), the decoder MLPs, and camera poses for the selected W frames. For tracking, we perform pose estimation for every incoming frame.

3.3 3DGS-based Pipeline

Driven by the same principles, we propose a second version of DINO-SLAM built over 3DGS, shown in Figure 4 (b)

Scene Representation. Following vanilla 3DGS, the scene is represented through a set of anisotropic Gaussians ζ where each Gaussian primitive ζ^i is characterized by its

Method	Acc.(cm)↓	Comp.(cm)↓	Comp.rate(%)↑	Depth L1(cm)↓	RMSE(cm)↓
iMAP	3.62	4.93	80.51	4.64	7.64
NICE-SLAM	2.37	2.65	91.14	1.90	2.50
Co-SLAM	2.10	2.08	93.44	1.51	0.86
ESLAM	2.18	1.75	96.46	0.94	0.63
PLGSLAM†	2.14	1.74	96.24	0.83	0.63
Point-SLAM	1.41	3.10	88.89	0.44	0.52
DINO-SLAM (NeRF)	1.94	1.64	97.06	0.66	0.51

Method	PSNR↑	SSIM↑	LPIP↓	RMSE(cm)↓
SplaTAM	33.97	0.968	0.102	0.36
Gaussian-SLAM	38.90	0.993	0.069	0.31
MonoGS	38.94	0.968	0.070	0.32
GS-SLAM	34.27	0.975	0.082	0.50
DINO-SLAM (3DGS)	39.12	0.971	0.062	0.30

Table 1: **Tracking and mapping results on Replica.** We present comparative results for both our NeRF-based (**left**) and 3DGS-based (**right**) implementations. For fair reconstruction evaluation, all generated meshes undergo post-processing using the culling strategy described in (Wang, Wang, and Agapito 2023). Meshes marked with † were obtained directly from the original authors. The best results are highlighted as **first**, **second**, and **third**.

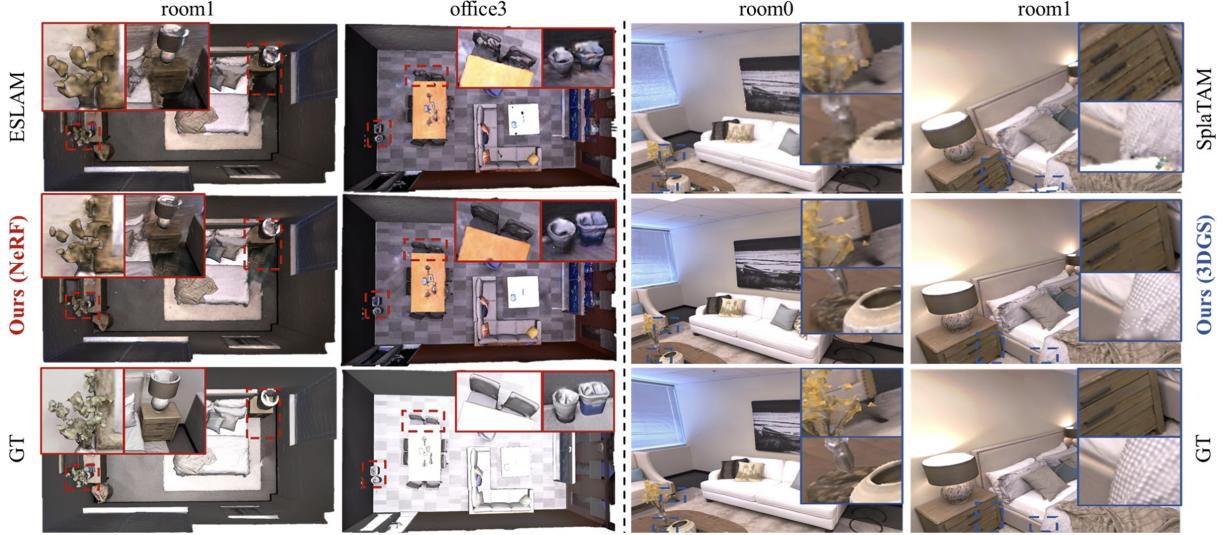


Figure 5: **Visualization of DINO-SLAM and baselines on the Replica.** We present details of **reconstruction** and **rendering** quality with **red boxes** and **blue boxes**. The two **left columns** present the reconstruction performance of our **DINO-SLAM (NeRF)**. Our method yields superior mesh results with detailed textures and better completeness. The two **right columns** show the rendering results of our **DINO-SLAM (3DGS)**. Our DINO-SLAM demonstrates high-fidelity and realistic images, especially around object boundaries.

parameters: color c^i , radius r^i , and opacity o^i . For continuous spatial representation, each Gaussian is further defined by its mean μ^i and covariance Σ^i , representing its position and ellipsoidal shape respectively. As shown in Figure 4 (b), we incorporate the EDINO features f_{ed} obtained from our SSE into each Gaussian’s parameters, while the raw DINO features extracted from images guide the optimization of the scene representation, emulating the NeRF-based pipeline introduced in the previous section. Specifically, each Gaussian ς^i corresponds to an embedding in the EDINO feature map. We assign its associated feature f_{ed}^i into the distinct channel of Gaussian ς^i parameters. This enhanced representation can be formalized through a modified Gaussian equation as follows:

$$\varsigma(x) = o \exp\left(-\frac{\|x - \mu\|^2}{2r^2}\right) \quad (10)$$

DINO-informed Rasterization. Following (Matsuki et al. 2024), our approach employs iterative rasterization over Gaussians instead of per-pixel ray casting. During rasterization, we project 3D Gaussians onto the image plane to

obtain 2D Gaussians through:

$$\mu_{2d} = \pi(T_{CW} \cdot \mu), \Sigma_{2d} = JW\Sigma W^T J^T \quad (11)$$

where μ_{2d} and Σ_{2d} represent the position and the covariance of 2D Gaussians, respectively. π denotes the projection operation and T_{CW} is the camera pose of the viewpoint. J is the Jacobian of the linear approximation of the projective transformation, and W is the rotational component of T_{CW} . Through splatting and blending N Gaussians, we can obtain the rendered feature map f'_d that captures enriched geometric and appearance information:

$$f'_d = \sum_{i \in N} f_{ed}^i \varsigma^i \prod_{j=1}^{i-1} (1 - \varsigma^j) \quad (12)$$

Similarly, we obtain color C and depth D through:

$$C = \sum_{i \in N} c^i \varsigma^i \prod_{j=1}^{i-1} (1 - \varsigma^j), D = \sum_{i \in N} z^i \varsigma^i \prod_{j=1}^{i-1} (1 - \varsigma^j) \quad (13)$$

where z^i is the distance to μ along the camera ray.

DINO-informed Supervision. We introduce a DINO-feature loss L_{df} to guide the optimization of the enriched

Method	Encodings	0000	0059	0106	0169	0181	0207	Avg.
iMAP	MLP	55.9	32.0	17.5	70.5	32.1	11.9	36.7
NICE-SLAM	Hier.Grid	12.0	14.0	7.9	10.9	13.4	6.2	10.7
Co-SLAM	Hash Grid	7.1	11.1	9.4	5.9	11.8	7.1	8.7
ESLAM	Tri-planes	7.3	8.5	7.5	6.5	9.0	5.7	7.4
PLGSLAM†	Tri-planes	-	-	-	-	-	-	6.8
Point-SLAM	Neu.Points	10.2	7.8	8.7	22.2	14.8	9.5	12.2
DINO-SLAM (NeRF)	Tri-planes	7.8	7.8	7.3	6.0	8.9	4.7	7.1
SplaTAM	3DGS	12.8	10.1	17.7	12.1	11.1	7.5	11.9
Gaussian-SLAM	3DGS	21.2	12.8	13.5	16.3	21.0	14.3	16.5
MonoGS	3DGS	9.8	32.1	8.9	10.7	21.8	7.9	15.2
DINO-SLAM (3DGS)	3DGS	12.9	6.4	8.4	9.5	11.3	8.8	9.5

Table 2: **Tracking results on ScanNet.** Avg. denotes the average ATE RMSE on the 6 scenes. Tetra. means the tetrahedron feature encoding.

scene representation. As illustrated in Figure 4 (b), this loss function measures the feature similarity between the DINO features f_d and the rendered feature maps f'_d :

$$L_{df} = \|f'_d - f_d\|_1 \quad (14)$$

Similarly, we define color loss and depth loss for the appearance and geometric optimization:

$$L_c = \|C - C_{gt}\|_1, L_d = \|D - D_{gt}\|_1 \quad (15)$$

where C_{gt} and D_{gt} represent the ground truth color and depth, respectively.

Mapping and Tracking. For mapping and tracking, we adopt the keyframe selection strategy based on co-visibility from (Li et al. 2024). The tracking thread focuses solely on camera pose optimization using color and depth residuals. In the mapping thread, we implement a global bundle adjustment (BA) to address both the forgetting problem and camera drift during significant movements. Following (Matsuki et al. 2024), we measure frame-to-frame motion using optical center distance d and parallax angle r . When significant motion occurs, d and r increase dramatically. Therefore, keyframes are selected when these metrics exceed their respective thresholds d_l and r_l (we set $d_l=0.7$ and $r_l=15$).

4 Experiments

We now discuss the outcome of our experiments.

Datasets. We conduct our evaluation across three standard datasets: Replica (Straub et al. 2019), ScanNet (Dai et al. 2017), and TUM RGB-D (Sturm et al. 2012). Replica provides photo-realistic indoor scenes specifically designed for evaluating dense reconstruction quality. ScanNet offers extensively annotated real-world data across diverse indoor environments, ranging from small rooms to large scenes. The TUM RGB-D benchmark, instead, features small-scale indoor scenes captured with an external camera system, providing high-precision ground truth trajectories.

Baselines. To fully assess the capabilities of DINO-SLAM, we compare against state-of-the-art methods, focusing on dense mapping, novel view synthesis, and camera tracking. Furthermore, we demonstrate the applicability of our DINO-SLAM design strategy by integrating it with various scene encoding approaches, including hash-tables (Wang, Wang, and Agapito 2023), tri-planes (Johari, Carta, and Fleuret 2023), neural points (Sandström et al. 2023), and 3D Gaussian Splatting (Keetha et al. 2024; Matsuki et al.

Method	Encodings	fr1_desk	fr2_xyz	fr3_office	Avg.
iMAP	MLP	4.90	2.00	5.80	4.23
NICE-SLAM	Hier.Grid	2.70	1.80	3.00	2.50
Co-SLAM	Hash Grid	2.40	1.70	2.40	2.17
ESLAM	Tri-planes	2.47	1.11	2.42	2.00
Point-SLAM	Neu.Points	4.34	1.31	3.48	3.04
DINO-SLAM (NeRF)	Tri-planes	2.43	1.14	2.29	1.95
SplaTAM	3DGS	3.35	1.24	5.16	3.27
Gaussian-SLAM	3DGS	2.60	1.30	4.60	2.83
MonoGS	3DGS	1.50	1.44	1.49	1.47
GS-SLAM	3DGS	3.30	1.30	6.60	3.73
DINO-SLAM (3DGS)	3DGS	1.57	1.01	1.50	1.36

Table 3: **Tracking results on TUM.** Avg. denotes the average ATE RMSE on the 3 scenes.

2024), thereby validating the effectiveness and generality of our approach.

Metrics. For quantitative evaluation, we adopt standard SLAM metrics (Tosi et al. 2024): Absolute Trajectory Error (ATE) RMSE for tracking accuracy, and reconstruction quality metrics including *accuracy (cm)*, *completion (cm)*, *completion rate (%)*, *depth ll (cm)*. Novel view rendering quality is assessed using *PSNR (dB)*, *SSIM*, and *LPIPS*.

Implementation Details. All experiments were conducted on a desktop PC equipped with an NVIDIA A100 GPU. For our 3DGS-based pipeline, we maintain consistency with the original Gaussian Splatting implementation (Kerbl et al. 2023), and set the DINO-feature loss weight to 1. In our NeRF-based pipeline, we employ a multi-resolution approach with geometry tri-planes at 24cm/6cm resolution and appearance/DINO tri-planes at 24cm/3cm resolution. The loss weights are configured as 5.0 for encoding feature loss and 0.01 for DINO-feature loss.

4.1 Comparison with state-of-the-art

Results on Replica. We begin our experiments on Replica, running our pipelines on 8 diverse scenes following standard practice in the literature. Table 1 compares our DINO-SLAM variants against state-of-the-art SLAM approaches. The table is divided into two sections: the left presents reconstruction and tracking results for NeRF-based methods, while the right shows rendering and tracking performance for 3DGS-based methods. All reported values represent averages across the test scenes. The results highlight the effectiveness of our DINO-SLAM paradigms. In particular, our 3DGS-based variant achieves state-of-the-art performance in both rendering quality and tracking accuracy among all 3DGS-based methods. Similarly, our NeRF-based implementation excels in completion, completion rate, and RMSE metrics, while remaining competitive in accuracy and depth L1 error. Figure 5 collects qualitative results that further validate the superiority of DINO-SLAM. The meshes produced by our NeRF-based variant (left two columns) demonstrate superior surface detail preservation while successfully completing previously missing regions. The rendering results of our 3DGS-based variant (right two columns) show photo-realistic rendering quality with significantly improved texture detail resolution.

Results on ScanNet. Our evaluation extends to ScanNet, where we test both DINO-SLAM variants on six sequences of varying complexity, including challenging long

Methods	Encoding	Acc.↓	Comp.↓	Comp.rate↑	Depth L1↓	RMSE(cm)↓
Co-SLAM	Hash-grid	2.10	2.08	93.44	1.51	0.86
+DINO	Hash-grid	2.02	2.08	93.55	1.44	0.81
ESLAM	Tri-planes	2.18	1.75	96.46	0.94	0.63
+DINO	Tri-planes	1.94	1.64	97.06	0.66	0.51
SNI-SLAM*	Tri-planes	1.94	1.70	96.62	0.77	0.46
+DINO	Tri-planes	1.86	1.63	96.98	0.70	0.43
Methods	Encoding	F1↑	Pre.↑	Recall↑	Depth L1↓	RMSE(cm)↓
Point-SLAM	Neur-points	89.77	96.99	83.59	0.44	0.52
+DINO	Neur-points	90.77	98.33	84.3	0.41	0.46
Methods	Encoding	PSNR↑	SSIM↑	LPIPS↓	Depth L1↓	RMSE(cm)↓
SplaTAM	3DGS	34.11	0.97	0.1	0.73	0.36
+DINO	3DGS	34.31	0.97	0.1	0.67	0.34
MonoGS	3DGS	38.94	0.97	0.07	0.49	0.32
+DINO	3DGS	39.10	0.97	0.06	0.47	0.30

Table 4: **Ablation study – DINO-SLAM generality.** We report some baselines and their DINO-extended variants, maintaining the same evaluation metrics reported in the original papers. * uses ground-truth semantic masks.

Component	Acc.↓	Comp.↓	Comp.rate↑	Depth L1↓	RMSE(cm)↓
(A) w/o DINO	2.18	1.75	96.46	0.94	0.63
(B) w/o EDINO	2.07	1.67	96.63	0.79	0.58
DINO-SLAM (NeRF)	1.94	1.64	97.06	0.66	0.51
Component	PSNR↑	SSIM↑	LPIPS↓	Depth L1↓	RMSE(cm)↓
(C) w/o DINO	21.43	0.78	0.41	0.49	12.67
(D) w/o EDINO	21.46	0.78	0.39	0.48	11.39
(E) w/o BA	21.49	0.78	0.39	0.47	13.18
DINO-SLAM (3DGS)	21.50	0.79	0.39	0.47	9.55

Table 5: **Ablation study – impact of single components.** We study the impact of key components on mapping and tracking accuracy. The NeRF-based pipeline runs on the Replica dataset to evaluate reconstruction and camera tracking (**upper**). The 3DGS-based pipeline is evaluated on the more challenging ScanNet dataset to test camera tracking and rendering quality (**lower**).

trajectories exceeding 5000 frames. As shown in Table 2, our 3DGS-based pipeline significantly outperforms existing 3DGS-based systems. Moreover, our NeRF-based pipeline surpasses most baselines on camera tracking. We note that PLGSLAM achieves slightly better results due to its design being specifically tailored for larger scene reconstruction, whereas our contribution is orthogonal to it and could potentially be integrated with such framework as well.

Results on TUM. To further validate our approach, we evaluate on three widely-used sequences from the TUM RGB-D dataset, including both short and long trajectories. As shown in Table 3, both implementations of DINO-SLAM achieve superior pose estimation accuracy, consistently outperforming all existing methods. These results confirm that our DINO-SLAM pipelines excel across all standard benchmarks commonly adopted in the field.

4.2 Ablation Experiments

We conduct ablation studies to demonstrate the versatility of DINO-SLAM and the impact of each component.

DINO-SLAM Generality. We prove the wide applicability of DINO-SLAM by integrating our SSE across various neural implicit and explicit representations: hash grid, tri-planes, neural points, and 3D Gaussian Splatting. Table 4 shows consistent performance improvements on Replica across all encoding architectures when augmented with our SSE. Moreover, we also demonstrate how our paradigm can further enhance the performance of those SLAM methods already relying on higher-level semantic cues, such as SNI-

Method	Encodings	Size(MB)↓	FPS↑
Co-SLAM	Hash-grid	6.7	7.97
Point-SLAM	Neu.Points	54.8	0.23
ESLAM	Tri-planes	27.2	4.62
SNI-SLAM	Tri-planes	52.1	0.61
Ours (NeRF)	Tri-planes	48.7	2.55
MonoGS	3DGS	28.5	0.62
SplaTAM	3DGS	265.3	0.14
SGS-SLAM	3DGS	312.4	0.13
Ours (3DGS)	3DGS	27.8	0.61

Table 6: **Memory usage and runtime** on Replica *room0*.

SLAM. The performance gains validate both the broad applicability of our SSE and the importance of DINO features for enhancing neural representations, suggesting the potential to extend our methodology to future SLAM systems based on either NeRF or 3DGS.

Components Analysis. We conducted an exhaustive ablation study to assess the effectiveness of the key components in DINO-SLAM pipelines, and report the results in Table 5. For the NeRF-based pipeline, we assessed reconstruction and camera tracking performance on the Replica dataset, while for the 3DGS-based pipeline we evaluate the accuracy of estimated poses, as well as the rendering quality on the more challenging ScanNet dataset.

The results reveal several key insights: first, removing DINO features entirely (A, C) yields substantial performance degradation across mapping, rendering, and tracking metrics, demonstrating the key role of DINO cues for enhanced scene representation and camera tracking. Additionally, when removing EDINO features – i.e., retaining raw DINO features only (B, D) – we observe improvements, although consistently lower performance across all metrics compared to our full system. This finding confirms that the improved performance is not only due to the raw DINO representations, but also from EDINO features enriched by the inter-relationships between DINO, appearance, and geometry features, thus establishing our SSE as the key component of DINO-SLAM. Finally, the removal of the global BA strategy (E) yields unsatisfactory tracking results, proving its effectiveness on the large scene dataset, particularly in challenging scenarios involving significant camera movements.

4.3 Performance Analysis

We compare our DINO-SLAM pipelines with NeRF-based and 3DGS-based baselines in both FPS (average time required to process per frame in a sequence) and memory usage (total footprint of the encoder and decoder). As shown in Table 6, Co-SLAM is the fastest method, yet its reconstruction accuracy is significantly lower than our NeRF-based SLAM. In contrast, our DINO-SLAM (NeRF) achieves faster speed with a smaller model compared to Point-SLAM and SNI-SLAM. Besides, our DINO-SLAM (3DGS) shows faster speed with the smallest model compared to MonoGS, SplaTAM, and SGS-SLAM.

5 Conclusion

We present DINO-SLAM, a DINO-informed dense RGB-D SLAM system that enhances both neural implicit and explicit representations. We implement two foundational

paradigms for both NeRF-based and 3DGS-based SLAM systems, built on top of our SSE capturing hierarchical scene layouts and structural relationships. Extensive experiments are conducted to validate the wide applicability and superior performance of our method. In future work, we will extend DINO-SLAM with more advanced components such as loop-closure and sub-mapping.

References

- Campos, C.; Elvira, R.; Rodríguez, J. J. G.; Montiel, J. M.; and Tardós, J. D. 2021. Orb-slam3: An accurate open-source library for visual, visual-inertial, and multimap slam. *IEEE transactions on robotics*, 37(6): 1874–1890.
- Caron, M.; Touvron, H.; Misra, I.; Jégou, H.; Mairal, J.; Bojanowski, P.; and Joulin, A. 2021. Emerging properties in self-supervised vision transformers. In *Proceedings of the IEEE/CVF international conference on computer vision*, 9650–9660.
- Dai, A.; Chang, A. X.; Savva, M.; Halber, M.; Funkhouser, T.; and Nießner, M. 2017. Scannet: Richly-annotated 3d reconstructions of indoor scenes. In *Proceedings of the IEEE conference on computer vision and pattern recognition*, 5828–5839.
- Deng, T.; Shen, G.; Qin, T.; Wang, J.; Zhao, W.; Wang, J.; Wang, D.; and Chen, W. 2024. Plgslam: Progressive neural scene representation with local to global bundle adjustment. In *Proceedings of the IEEE/CVF Conference on Computer Vision and Pattern Recognition*, 19657–19666.
- Gong, Z.; Tosi, F.; Zhang, Y.; Mattoccia, S.; and Poggi, M. 2025. HS-SLAM: Hybrid Representation with Structural Supervision for Improved Dense SLAM. In *Proceedings of the IEEE International Conference on Robotics and Automation (ICRA)*.
- Ha, S.; Yeon, J.; and Yu, H. 2024. Rgb-d gs-icp slam. In *European Conference on Computer Vision*, 180–197. Springer.
- Hu, J.; Chen, X.; Feng, B.; Li, G.; Yang, L.; Bao, H.; Zhang, G.; and Cui, Z. 2024. Cg-slam: Efficient dense rgb-d slam in a consistent uncertainty-aware 3d gaussian field. In *European Conference on Computer Vision*, 93–112. Springer.
- Hu, J.; Mao, M.; Bao, H.; Zhang, G.; and Cui, Z. 2023. Cp-slam: Collaborative neural point-based slam system. *Advances in Neural Information Processing Systems*, 36: 39429–39442.
- Huang, H.; Li, L.; Cheng, H.; and Yeung, S.-K. 2024. Photoslam: Real-time simultaneous localization and photorealistic mapping for monocular stereo and rgb-d cameras. In *Proceedings of the IEEE/CVF Conference on Computer Vision and Pattern Recognition*, 21584–21593.
- Johari, M. M.; Carta, C.; and Fleuret, F. 2023. Eslam: Efficient dense slam system based on hybrid representation of signed distance fields. In *Proceedings of the IEEE/CVF Conference on Computer Vision and Pattern Recognition*, 17408–17419.
- Keetha, N.; Karhade, J.; Jatavallabhula, K. M.; Yang, G.; Scherer, S.; Ramanan, D.; and Luiten, J. 2024. SplatAM: Splat Track & Map 3D Gaussians for Dense RGB-D SLAM. In *Proceedings of the IEEE/CVF Conference on Computer Vision and Pattern Recognition*, 21357–21366.
- Kerbl, B.; Kopanas, G.; Leimkühler, T.; and Drettakis, G. 2023. 3d gaussian splatting for real-time radiance field rendering. *ACM Trans. Graph.*, 42(4): 139–1.
- Li, G.; Chen, Q.; Yan, Y.; and Pu, J. 2024. EC-SLAM: Effectively Constrained Neural RGB-D SLAM with Sparse TSDF Encoding and Global Bundle Adjustment. *arXiv preprint arXiv:2404.13346*.
- Li, Y.; Brasch, N.; Wang, Y.; Navab, N.; and Tombari, F. 2020. Structure-slam: Low-drift monocular slam in indoor environments. *IEEE Robotics and Automation Letters*, 5(4): 6583–6590.
- Liso, L.; Sandström, E.; Yugay, V.; Van Gool, L.; and Oswald, M. R. 2024. Loopy-slam: Dense neural slam with loop closures. In *Proceedings of the IEEE/CVF Conference on Computer Vision and Pattern Recognition*, 20363–20373.
- Matsuki, H.; Murai, R.; Kelly, P. H.; and Davison, A. J. 2024. Gaussian splatting slam. In *Proceedings of the IEEE/CVF Conference on Computer Vision and Pattern Recognition*, 18039–18048.
- Mildenhall, B.; Srinivasan, P. P.; Tancik, M.; Barron, J. T.; Ramamoorthi, R.; and Ng, R. 2021. Nerf: Representing scenes as neural radiance fields for view synthesis. *Communications of the ACM*, 65(1): 99–106.
- Mur-Artal, R.; Montiel, J. M. M.; and Tardós, J. D. 2015. ORB-SLAM: A Versatile and Accurate Monocular SLAM System. *IEEE Transactions on Robotics*, 31(5): 1147–1163.
- Mur-Artal, R.; and Tardós, J. D. 2017. Orb-slam2: An open-source slam system for monocular, stereo, and rgb-d cameras. *IEEE transactions on robotics*, 33(5): 1255–1262.
- Newcombe, R. A.; Lovegrove, S. J.; and Davison, A. J. 2011. DTAM: Dense tracking and mapping in real-time. In *2011 international conference on computer vision*, 2320–2327. IEEE.
- Park, H.; Park, M.; Nam, G.; and Kim, J. 2024. LRSLAM: Low-Rank Representation of Signed Distance Fields in Dense Visual SLAM System. In *European Conference on Computer Vision*, 225–240. Springer.
- Peng, Z.; Shao, T.; Liu, Y.; Zhou, J.; Yang, Y.; Wang, J.; and Zhou, K. 2024. Rtg-slam: Real-time 3d reconstruction at scale using gaussian splatting. In *ACM SIGGRAPH 2024 Conference Papers*, 1–11.
- Salas-Moreno, R. F.; Newcombe, R. A.; Strasdat, H.; Kelly, P. H.; and Davison, A. J. 2013. Slam++: Simultaneous localisation and mapping at the level of objects. In *Proceedings of the IEEE conference on computer vision and pattern recognition*, 1352–1359.
- Sandström, E.; Li, Y.; Van Gool, L.; and Oswald, M. R. 2023. Point-slam: Dense neural point cloud-based slam. In *Proceedings of the IEEE/CVF International Conference on Computer Vision*, 18433–18444.
- Straub, J.; Whelan, T.; Ma, L.; Chen, Y.; Wijmans, E.; Green, S.; Engel, J. J.; Mur-Artal, R.; Ren, C.; Verma, S.; et al. 2019. The replica dataset: A digital replica of indoor spaces. *arXiv preprint arXiv:1906.05797*.

Sturm, J.; Engelhard, N.; Endres, F.; Burgard, W.; and Cremers, D. 2012. A benchmark for the evaluation of RGB-D SLAM systems. In *2012 IEEE/RSJ international conference on intelligent robots and systems*, 573–580. IEEE.

Sucar, E.; Liu, S.; Ortiz, J.; and Davison, A. J. 2021. imap: Implicit mapping and positioning in real-time. In *Proceedings of the IEEE/CVF international conference on computer vision*, 6229–6238.

Tateno, K.; Tombari, F.; Laina, I.; and Navab, N. 2017. Cnn-slam: Real-time dense monocular slam with learned depth prediction. In *Proceedings of the IEEE conference on computer vision and pattern recognition*, 6243–6252.

Teed, Z.; and Deng, J. 2021. DROID-SLAM: Deep Visual SLAM for Monocular, Stereo, and RGB-D Cameras. In *Advances in neural information processing systems*.

Tosi, F.; Zhang, Y.; Gong, Z.; Sandström, E.; Mattoccia, S.; Oswald, M. R.; and Poggi, M. 2024. How nerfs and 3d gaussian splatting are reshaping slam: a survey. *arXiv preprint arXiv:2402.13255*, 4: 1.

Wang, H.; Wang, J.; and Agapito, L. 2023. Co-slam: Joint coordinate and sparse parametric encodings for neural real-time slam. In *Proceedings of the IEEE/CVF Conference on Computer Vision and Pattern Recognition*, 13293–13302.

Xin, Z.; Yue, Y.; Zhang, L.; and Wu, C. 2024. Hero-slam: Hybrid enhanced robust optimization of neural slam. In *2024 IEEE International Conference on Robotics and Automation (ICRA)*, 8610–8616. IEEE.

Yan, C.; Qu, D.; Xu, D.; Zhao, B.; Wang, Z.; Wang, D.; and Li, X. 2024. Gs-slam: Dense visual slam with 3d gaussian splatting. In *Proceedings of the IEEE/CVF Conference on Computer Vision and Pattern Recognition*, 19595–19604.

Yugay, V.; Li, Y.; Gevers, T.; and Oswald, M. R. 2023. Gaussian-slam: Photo-realistic dense slam with gaussian splatting. *arXiv preprint arXiv:2312.10070*.

Zhang, Y.; Tosi, F.; Mattoccia, S.; and Poggi, M. 2023. Go-slam: Global optimization for consistent 3d instant reconstruction. In *Proceedings of the IEEE/CVF International Conference on Computer Vision*, 3727–3737.

Zheng, J.; Zhu, Z.; Bieri, V.; Pollefeys, M.; Peng, S.; and Armeni, I. 2025. Wildgs-slam: Monocular gaussian splatting slam in dynamic environments. In *Proceedings of the Computer Vision and Pattern Recognition Conference*, 11461–11471.

Zhu, Z.; Peng, S.; Larsson, V.; Xu, W.; Bao, H.; Cui, Z.; Oswald, M. R.; and Pollefeys, M. 2022. Nice-slam: Neural implicit scalable encoding for slam. In *Proceedings of the IEEE/CVF conference on computer vision and pattern recognition*, 12786–12796.